Journal of Magnetism and Magnetic Materials 498 (2020) 166168

Contents lists available at ScienceDirect

Journal of Magnetism and Magnetic Materials

journal homepage: www.elsevier.com/locate/jmmm

Research articles

Microstructure, porosity and magnetic properties of $Zn_{0.5}Co_{0.5}Fe_2O_4/SiO_2$ nanocomposites prepared by sol-gel method using different polyols

Thomas Dippong[a,*], Oana Cadar[b], Erika Andrea Levei[b], Iosif Grigore Deac[c]

[a] Technical University of Cluj-Napoca, North University Center of Baia Mare, Department of Chemistry and Biology, 76 Victoriei Street, 430122 Baia Mare, Romania
[b] INCDO-INOE 2000, Research Institute for Analytical Instrumentation, 67 Donath Street, 400293 Cluj-Napoca, Romania
[c] Babes-Bolyai University, Faculty of Physics, 1 Kogalniceanu Street, 400084 Cluj-Napoca, Romania

ARTICLE INFO

Keywords:
Magnetic ceramics
Zn-Co ferrite
Polyol
Nanocomposites
Magnetic properties

ABSTRACT

The study reports the influence of polyols (1,2-ethanediol, 1,2-propanediol, 1,3-propanediol, 1,2,3-propanetriol) used in the synthesis on the structure and magnetic properties of $Zn_{0.5}Co_{0.5}Fe_2O_4/SiO_2$ nanocomposites. The X-ray diffraction patterns indicated the formation of poorly to highly crystalline $Zn_{0.5}Co_{0.5}Fe_2O_4$, together with several other crystalline phases (Zn_2SiO_4, Co_2SiO_4, SiO_2, Co_3O_4, ZnO), depending on the used polyol and annealing temperature. The Fourier transformed infrared spectra confirmed the formation of metal oxide bonds in Co-Zn ferrite and of SiO_2 matrix. The physical density increases and the X-ray density decreases with average crystallite size decrease. The transmission electron microscopy measurements revealed the spherical nanoparticles (2–47 nm) size growth with increasing distance between the hydroxyl groups and number of hydroxyl groups. The shape of the hysteresis loops suggests the dependence of the magnetic behaviour on the structural properties, and consequently, on the polyol structure and the annealing temperature. Also, the saturation magnetization (M_s, ~ 15.8–61.0 emu/g), remanent magnetization (M_R ~ 0.41–9.5 emu/g) and coercive field (H_c ~ 0.014–0.021 T) of $Zn_{0.5}Co_{0.5}Fe_2O_4$ increase with the polyol chain length and hydroxyl group number. Both M_s and H_c increase with increasing crystallite size. The shape of the magnetization derivative curves with respect to the applied magnetic field indicates the presence of a single magnetic phase ($Zn_{0.5}Co_{0.5}Fe_2O_4$) that has ferromagnetic or superparamagnetic type behaviour, depending on the annealing temperature.

1. Introduction

Recently, a wide range of semiconductor magnetic ceramic nanomaterials with applicability in photocatalysis, electronics, optoelectronics, data and energy storage, ceramics, ion sensing and medicine were prepared [1–9]. Mixed zinc-cobalt ferrites (ZCFs) are widely studied because of their excellent chemical stability, good mechanical properties, very high resistivity and magnetocrystalline anisotropy, low cost and easy manufacturing process. These features make ZCFs suitable for many applications such as magnetic recording, supercapacitors, photo-magnetic devices, optoelectronics, transformer cores and catalysis [10–15].

ZCF based nanocomposites (NCs) have been prepared using various methods such as coprecipitation, sol–gel, reverse micelle, microemulsion, hydrothermal-assisted homogenous precipitation, solvothermal, forced hydrolysis, sol–gel method, citrate-gel solution combustion, auto-combustion, microwaving and ball milling, laser deposition and thermal decomposition methods [11,16–19]. The physical, chemical and magnetic properties of ZCF strongly depend on synthesis route, particle size, composition, morphology, cation distribution, coating and doping by a magnetic or nonmagnetic material [20–24]. The sol–gel method has the advantage of producing high purity NCs at low temperatures and allows a precise microstructural and chemical control. Moreover, is a simple and cost-effective method. The major disadvantage of this method is the obtaining of dense, small particle sized ferrites even at relatively low temperatures [23].

ZCFs can behave both like hard or soft magnets. Hard ferrites have a high remanent magnetization (M_R) and high coercivity (H_c) and are mainly used as permanent magnets [13]. Soft ferrites have narrow magnetic hysteresis loops, very low M_R and H_c, and large permeability values in a wide frequency range [13,21,25]. The lowering of magnetization is attributed to the presence of local disordered surface spins and to the spin canting effect on the surface of the nanoparticles [21,26,27]. These effects have higher influence with decreasing particle size due to a high surface to volume ratio [19]. The H_c and magnetostriction were found to decrease with increasing Zn content in ZCFs as

* Corresponding author.
E-mail address: dippong.thomas@yahoo.ro (T. Dippong).

https://doi.org/10.1016/j.jmmm.2019.166168
Received 17 August 2019; Received in revised form 15 November 2019; Accepted 16 November 2019
Available online 18 November 2019
0304-8853/

the Zn^{2+} ions are non-magnetic and they dilute the magnetic lattice. Thus, the magnetic anisotropy decreases and the magnetic lattice become more sensitive to the strain [11]. Moreover, magnetic nanoparticles have the tendency to aggregate due to inter-particle interactions and to their high surface reactivity leading to a sort of collective magnetic behaviour which is different from that of non-agglomerated nanoparticles [19,28].

In our previous studies [29,30], we presented the effect of polyol on the structural, morphological and magnetic properties of Co-ferrite and mixed Co-Ni ferrite NCs. In the case of $CoFe_2O_4/SiO_2$ and $Ni_{0.5}Co_{0.5}Fe_2O_4/SiO_2$, at high temperature annealing (900–1000 °C) single phase ferrite was obtained, while at low temperatures (400–700 °C) beside the ferrites, metal oxides (Co_3O_4, NiO) were also obtained. The H_c was found to increase with increasing polyol chain length. In the present study, we follow the effect of polyol chain length and number of hydroxyl groups on the structure and magnetic properties of $Zn_{0.5}Co_{0.5}Fe_2O_4/SiO_2$ obtained by sol–gel method. A special emphasis was given to the influence of the polyol structure and annealing temperature on the crystallite size, lattice parameter size, physical density, X-ray density, porosity, saturation magnetization, coercivity and remanent magnetization. Moreover, the influence of Zn in the ferrite structure on the formation of crystalline phases, as a function of the polyol structure and annealing temperature was assessed.

2. Experimental

2.1. Synthesis

As Zn, Fe and Co sources, zinc nitrate ($Zn(NO_3)_2{\cdot}6H_2O$), iron nitrate ($Fe(NO_3)_3{\cdot}9H_2O$) and cobalt nitrate ($Co(NO_3)_2{\cdot}6H_2O$) were used. The 1,2-ethanediol (1.2ED), 1,2-propanediol (1.2PD), 1,3-propanediol (1.3PD), 1,2,3-propanetriol (1.2.3PT) were used as chelators, tetraethyl orthosilicate (TEOS) as silica source, while ethanol (EtOH) and HNO_3 as reaction media. All reagents were of analytical grade (Merck) and used without further purification. The sol was prepared by dissolving Zn $(NO_3)_2{\cdot}6H_2O$, $Co(NO_3)_2{\cdot}6H_2O$ and $Fe(NO_3)_3{\cdot}9H_2O$ in a molar ratio of 1:1:4, followed by the addition of the polyol (NO_3^-: polyol in molar ratio 1:1), at room temperature, in ethanolic solution, according to Table 1. HNO_3 was added to adjust the acidity. Subsequently, an amount of TEOS equal to 50% of the weight of Zn(II), Co(II) and Fe(III) nitrates was added dropwise, under continuous magnetic stirring for 30 min. The resulting clear solution was exposed to open air for slow gelation. The time from synthesis to gelation is presented in Table 1. To obtain Zn-Co ferrite NCs, the gels were thermally treated at 400 °C for 4 h and afterwards annealed at 700 and 1000 °C for 4 h.

2.2. Characterization

The X-ray diffraction (XRD) measurements were performed at room temperature, using a Bruker D8 Advance diffractometer with $CuK_{??}$ radiation (?? = 1.54056 Å). The Fourier-transform infrared (FT-IR) spectra were recorded in transmission mode on 1% KBr pellets using a Perkin-Elmer Spectrum BX II spectrometer. The size, shape and clustering of nanoparticles were investigated using a Hitachi HD-2700 TEM equipped with digital image recording system and photographic film image with high resolution scanner using samples suspended onto carbon film coated copper grids. Based on TEM images, the particle's size distribution was determined using the ImageJ software according to the method presented by Rice et al. [31]. N_2 adsorption/desorption measurements, at the liquid nitrogen temperature (−196 °C) on degassed samples (200 °C, 2 Pa, 4 h) were used for the determination of the specific surface area (SSA) of ZCFs using a Thermo Electron Sorptomatic 1990 analyser. The magnetic measurements were performed using a vibrating sample cryogen-free Cryogenic Limited VSM magnetometer. The hysteresis loops were recorded in magnetic fields between −2 to 2 T, at room temperature, while the magnetization versus magnetic field measurements were performed to find M_S up to 5 T, on samples embedded in epoxy resin to prevent the nanoparticle movement.

3. Results and discussion

3.1. Structural characterization

The XRD patterns of NCs at 400, 700 and 1000 °C are shown in Fig. 1. For ZCF-1.2ED, crystalline Co_3O_4 (JCPDS card 80–1541) and ZnO (JCPDS card 89-1397) at 400 °C, poorly crystallized $Zn_{0.5}Co_{0.5}Fe_2O_4$ with similar structure to $CoFe_2O_4$ (JCPDS card 16-6200) and to $ZnFe_2O_4$ (JCPDS card 16–6205), Co_3O_4 and ZnO at 700 °C, while well-crystallized $Zn_{0.5}Co_{0.5}Fe_2O_4$ together with traces of Co_2SiO_4 (JCPDS card 79–0791), Zn_2SiO_4 (JCPDS card 01–1076) and SiO_2 (JCPDS card 89-8935) at 1000 °C were observed [32]. The profile line of $CoFe_2O_4$ and $ZnFe_2O_4$ (Fig. 1) is fitted for (1 1 1), (2 2 0), (3 1 1), (2 2 2), (4 0 0), (4 4 2), (5 1 1) and (4 4 0) reflection planes in $Zn_{0.5}Co_{0.5}Fe_2O_4$, indicating a cubic spinel ferrite belonging to *Fd3m* space group [33]. The presence of Co and Zn silicates at 1000 °C could be a consequence of the reaction between CoO, ZnO and SiO_2 that is thermodynamically more favoured than the formation of Zn-Co ferrite. The presence of Co_2SiO_4 at 1000 °C indicates the reduction of Co_3O_4 to CoO followed by the reaction of CoO with SiO_2 [34]. In case of ZCF-1.2PD and ZCF-1.3PD NCs, XRD patterns show only traces of Co_3O_4 at 400 °C, poorly crystallized Zn-Co ferrite and Co_3O_4 at 700 °C and crystalline cubic $Zn_{0.5}Co_{0.5}Fe_2O_4$ spinel together with secondary olivine (Co_2SiO_4) and willemite (Zn_2SiO_4) at 1000 °C. For ZCF-1.2.3PT, at 400 °C, poorly-crystallized Zn-Co ferrite, at 700 °C $Zn_{0.5}Co_{0.5}Fe_2O_4$ main and Co_3O_4 secondary phases, while at 1000 °C Zn-Co ferrite main phase together with Co_2SiO_4 and Zn_2SiO_4 secondary phases were identified.

The crystallite size is a very important factor that influences the magnetic and optical properties of NCs [12]. The average crystallite size is estimated by Debye-Scherrer's equation, based on the XRD data, using the full width at half maximum of the strongest reflection [30,35]. The crystallite size is influenced by the polyol used in the synthesis, by determining the saturation level during the nucleation-growth and crystallization. In our case the average crystallite size increases from 9.0 to 43.7 nm at 1000 °C [36–38]. By increasing the annealing temperature, the crystallite sizes increase, corresponding to narrow and sharp diffraction peaks, while the smaller crystallite size at lower temperatures cause a peak broadening [39]. The annealing temperature induces an increase of nucleation that further leads to more stable

Table 1
Synthesis route of ZCF-1,2ED, ZCF-1,2PD, ZCF-1,3PD si ZCF-1,2,3PT.

Sample	$Zn(NO_3)_2{\cdot}6H_2O$ (g)	$Co(NO_3)_2{\cdot}6H_2O$ (g)	$Fe(NO_3)_3{\cdot}9H_2O$ (g)	1,2-ED (mL)	1.2PD (mL)	1.3PD (mL)	1.2.3PT (mL)	TEOS (mL)	tgel* (days)
ZCF-1,2ED	29.8	29.1	16.2	110.6	–	–	–	311	11
ZCF-1,2PD	29.8	29.1	16.2	–	126.1	–	–	311	12
ZCF-1,3PD	29.8	29.1	16.2	–	–	128.2	–	311	12
ZCF-1,2,3PT	29.8	29.1	16.2	–	–	–	185.5	311	14

*t_{gel} – the time required to form a solid, glassy mass.

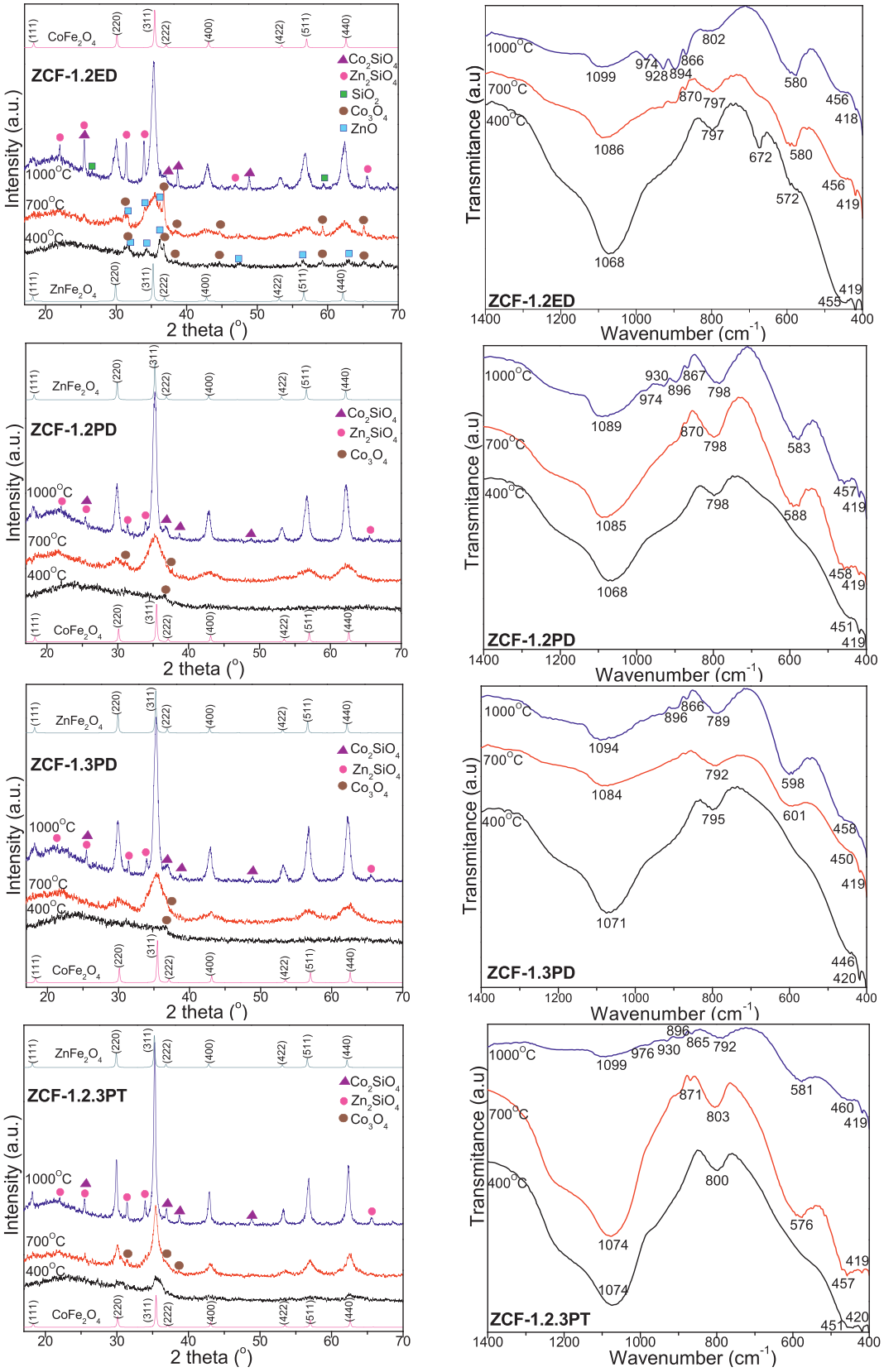

Fig. 1. XRD patterns and FT-IR spectra of $Zn_{0.5}Co_{0.5}Fe_2O_4/SiO_2$ NCs annealed at 400, 700 and 1000 °C.

particles [35]. At 1000 °C, a significant agglomeration take place without subsequent recrystallization, which favour the formation of a single crystal rather than a polycrystal [40,41].

The FT-IR spectra (Fig. 1) of gels annealed at 400, 700 and 1000 °C show the absorption bands attributed to the vibration of the crystal lattice [23]. In all cases, the absorption bands at 571–601 cm^{-1} and 418–420 cm^{-1} are attributed to stretching vibration of Co–O and Zn–O bonds, while the band at 446–460 cm^{-1} is assigned to Fe–O stretching

bond vibration of $Zn_{0.5}Co_{0.5}Fe_2O_4$ [42–44]. The presence of these absorption bands indicates the formation of spinel ferrite structure. For ZCF-1,2EG annealed at 400 and 700 °C, the band around 672 cm^{-1} is attributed to Co_3O_4 ($CoO{\cdot}Co_2O_3$), confirming that at low annealing temperatures, a high amount of CoO is obtained as suggested by the XRD results [45]. At 1000 °C, all samples show the characteristic vibrational modes of SiO_4, the band at 865–871 cm^{-1} attributed to symmetric stretching, bands of 894–896, 928–930 and 974–976 cm^{-1} attributed to asymmetric stretching and band of 446–460 cm^{-1} attributed to asymmetric deformation, confirming the formation of Co_2SiO_4 and Zi_2SiO_4 [46]. The formation of SiO_2 matrix is confirmed in all spectra, by the absorption bands at 789–803 cm^{-1} and 1068–1099 cm^{-1} correspond to symmetric and asymmetric stretching Si–O–Si vibrations [47]. The formation and decomposition of Fe-, Co- and Zn-carboxylate precursors and formation of ferrites studied by FT-IR and thermal analysis were presented in a previous study [48].

The lattice parameter (a) of each peak was calculated by using (Eq. (1)) [22,35].

$$a = d(h^2 + k^2 + l^2)^{1/2} \quad (1)$$

where h, k and l are Miller indices of the crystal planes and d is the interplanar distance of hkl planes.

The physical density (d_{phys}) of $Zn_{0.5}Co_{0.5}Fe_2O_4$ NCs annealed at 700 and 1000 °C was calculated by Archimedes method according to Eq. (2), the X-ray density (d_{XRD}) according to Eq. (3) while the percentage porosities (P) according to Eq. (4) [40]. The lowest d_{phys} value is attributed to the pore formation during synthesis processes [35].

$$d_{phys} = \frac{w \bullet \rho}{w - w'} \quad (2)$$

$$d_{XRD} = \frac{8 \bullet M_w}{N_A \bullet a^3} \quad (3)$$

$$P = \left(1 - \frac{d_{phys}}{d_{XRD}}\right)100 \quad (4)$$

where: w is the weight of the sample, in air (g), w' is the weight of the sample, in xylene (g), ρ is the density of xylene (g/cm^3), 8 is the number of molecules in the unit cell of spinel lattice, M_w is molecular weight (237.861 g/mol), N_A is Avogadro's number ($6.022{\cdot}10^{23}$/mol), a is the lattice parameter.

The increase of lattice parameter with the annealing temperature, the polyol chain length and the distance between hydroxyl groups (Table 2), indicate the lattice expansion without disturbing the lattice symmetry, in agreement with Vegard's law, indicating the formation of solid solution [14,15].

The value of d_{phys} increases, while d_{XRD} decreases with increasing distance between hydroxyl groups and number of hydroxyl groups. Moreover, d_{phys} increases, while d_{XRD} decrease with increasing crystallite size (Fig. 2). A possible explanation could be that in the equation of d_{XRD} and P, the lattice parameter has a significant influence, indicating that the lattice expands without disturbing the symmetry of lattice [40]. The increase of annealing temperature determines a decrease of both d_{phys} and d_{XRD}. The rapid densification during the annealing process leads to decrease of porosity with increasing distance of hydroxyl group and annealing temperature [40]. The low P values indicate a highly dense structure of ZCF-1.2.3PT NCs. The decrease of P (from 17.866% to 16.124%, at 1000 °C) with increasing physical density may be the result of the different grain size, while by annealing, the growth of the irregular shaped grains takes place [40].

At 700 °C, the porosity decreases exponentially with the crystallite sizes probably due to the low degree of crystallinity and porosity and non-equilibrium cation distribution in our samples [42]. This fact could suggest an incomplete annealing at 700 °C. However, after annealing at 1000 °C, well-defined linear relationship between porosity and crystallite sizes are remarked.

3.2. Morphology

The TEM images in Fig. 3 reveal spherical shaped ferrite nanoparticles, well dispersed in the matrix. The particles are well-separated at high and aggregated at low annealing temperatures. This aggregation may be due to the surface and interfacial tensions and to improper suspension during sample preparation [43]. The size of nanoparticles calculated from TEM images, were in the range of 7–47 nm and increase with the annealing temperature, the distance between hydroxyl groups and the number of hydroxyl groups. A possible explanation could be the growth rate of nanoparticles due to volume expansion and supersaturation reduction at high annealing temperatures [45]. At 400 °C, the structure is more amorphous than crystalline, with compact to strongly porous particles, at 700 °C the actual particle size is considered disregarding whether they are single crystal or not, while 1000 °C, the particles are well-separated [23,39]. However, with increasing annealing temperature there is a divergence between the crystallite size estimated by XRD and by TEM data (Table 2), probably due to the fact that the Scherrer formula considers only single crystals, while TEM the particle size [39]. Moreover, the interference of amorphous SiO_2 and large-size nanoparticles have important contribution to the diffraction patterns, as they contain a large fraction of the total number of atoms [47]. The nanoparticles size increases from 2 to 10 nm (400 °C), 7 to 30 nm (700 °C) and 20 to 47 nm (1000 °C) with increasing distance between hydroxyl groups and number of hydroxyl groups, under favourable energetic conditions, when particles come in contact with each other, some of them grow, while others decrease or disappear resulting a smaller number of large particles [47].

The particle size (D) distributions of ZCF-1.2ED, ZCF-1.2PD, ZCF-1.3PD and ZCF-1.2.3PT are presented in Fig. 4. The particle size variation with the annealing temperature could be explained by the incompletely crystallization of $Zn_{0.5}Co_{0.5}Fe_2O_4$ (at 700 °C) and the strong surface effect that easily gathers the low sized crystallites into larger aggregates (at 1000 °C). The NP sizes increase with annealing temperature as a result of the formation of crystalline clusters which become jointly cemented [47]. TEM confirms the influence of diol chain length on the particle size.

Table 2
Lattice parameter (a), average crystallite (D_c) from XRD and particle (D_p) size from TEM, physical density (d_{phys}), X-ray density (d_{XRD}) and porosity (P) of $Zn_{0.5}Co_{0.5}Fe_2O_4/SiO_2$ NCs at 700 and 1000 °C.

NCs	ZCF-1.2ED		ZCF-1.2PD		ZCF-1.3PD		ZCF-1.2.3PT	
Annealing temperature	700 °C	1000 °C	700 °C	1000 °C	700 °C	1000 °C	700 °C	1000 °C
a (Å)	8.342	8.375	8.354	8.385	8.363	8.395	8.378	8.412
D_c (nm)	4.1	9.8	8.1	16.1	13.1	26.5	27.4	43.7
D_p (nm)	7.0	12.0	11.0	20	21.0	32.0	30.0	47.0
d_{phys} (g/cm^3)	4.423	4.418	4.432	4.425	4.441	4.436	4.458	4.453
d_{XRD} (g/cm^3)	5.443	5.379	5.420	5.365	5.402	5.343	5.373	5.309
P (%)	18.740	17.866	18.229	17.522	17.790	16.981	17.030	16.124

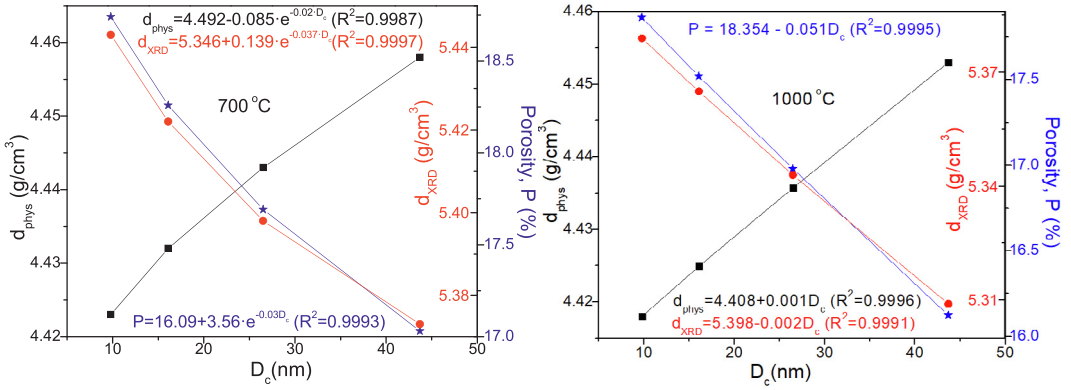

Fig. 2. Dependence of physical density (d_{phys}), X-ray density (d_{XRD}) and porosity (P) on crystallite size (D_c) of $Zn_{0.5}Co_{0.5}Fe_2O_4$ NCs annealed at 700 and 1000 °C.

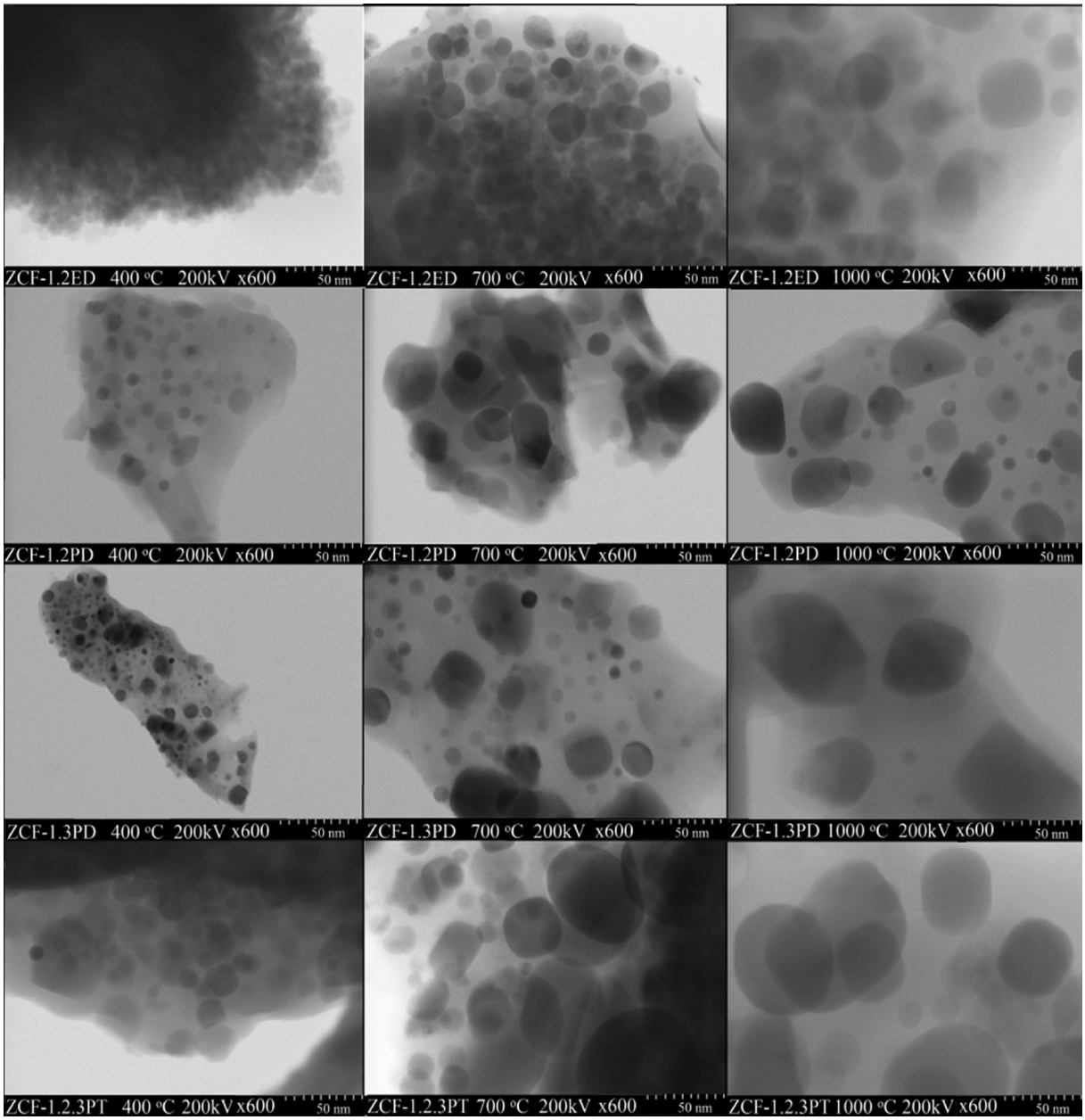

Fig. 3. TEM images of ZCF-1.2ED, ZCF-1.2PD, ZCF-1.3PD and ZCF-1.2.3PT annealed at 400, 700 and 1000 °C.

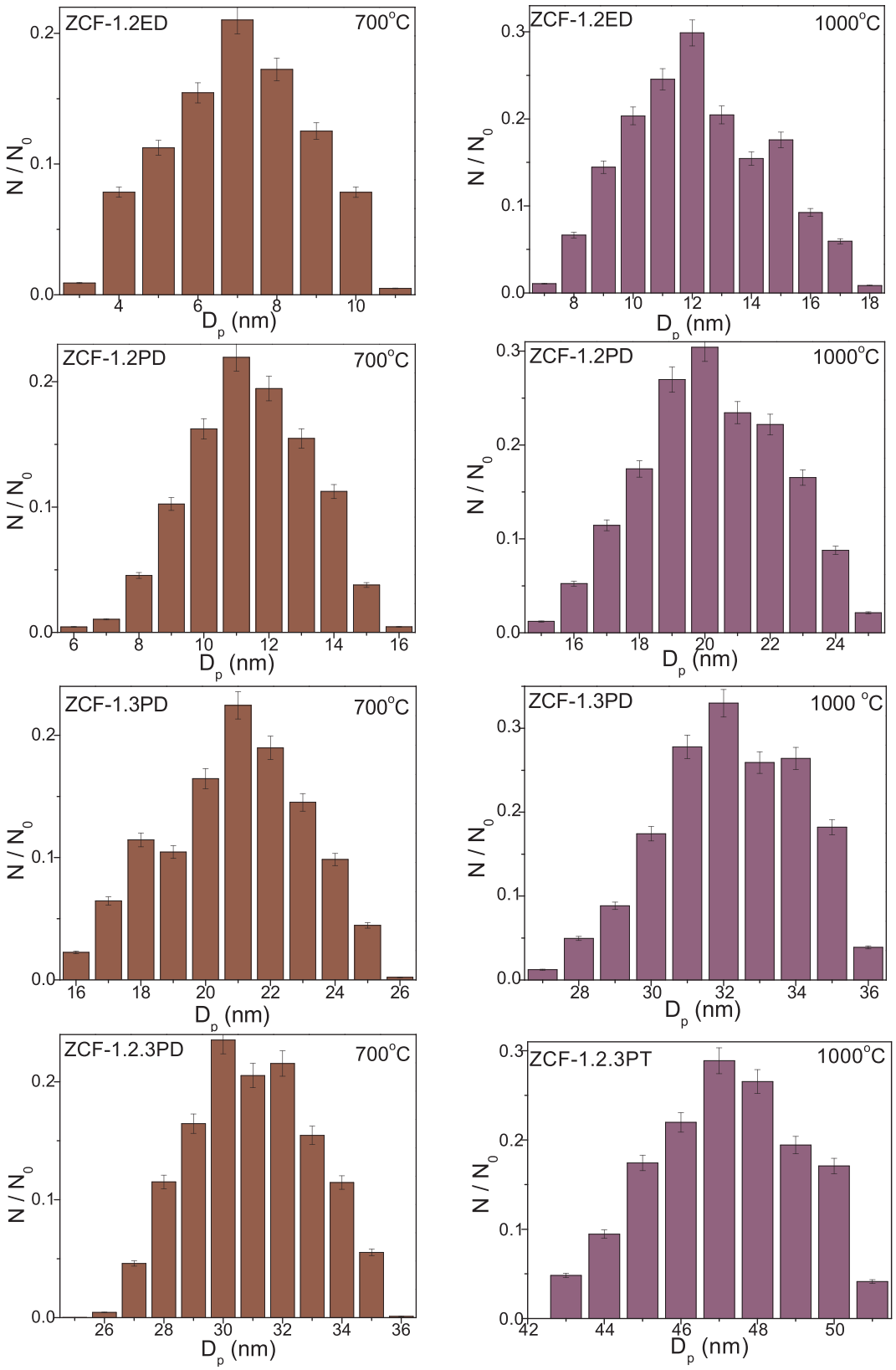

Fig. 4. Particle size distributions of ZCF-1.2ED, ZCF-1.2PD, ZCF-1.3PD and ZCF-1.2.3PT annealed at 700 and 1000 °C.

3.3. N_2 adsorption/desorption measurements

Due to the low adsorbed/desorbed N_2 amount, the adsorption/desorption measurements did not allow the determination of porosity and specific surface area (SSA) for samples annealed at 1000 °C. The SSA below the method detection limit (0.5 m^2/g), suggests that ZCF NCs have non-porous structure, probably as a consequence of samples agglomeration that limit the absorption of N_2 [49–51].

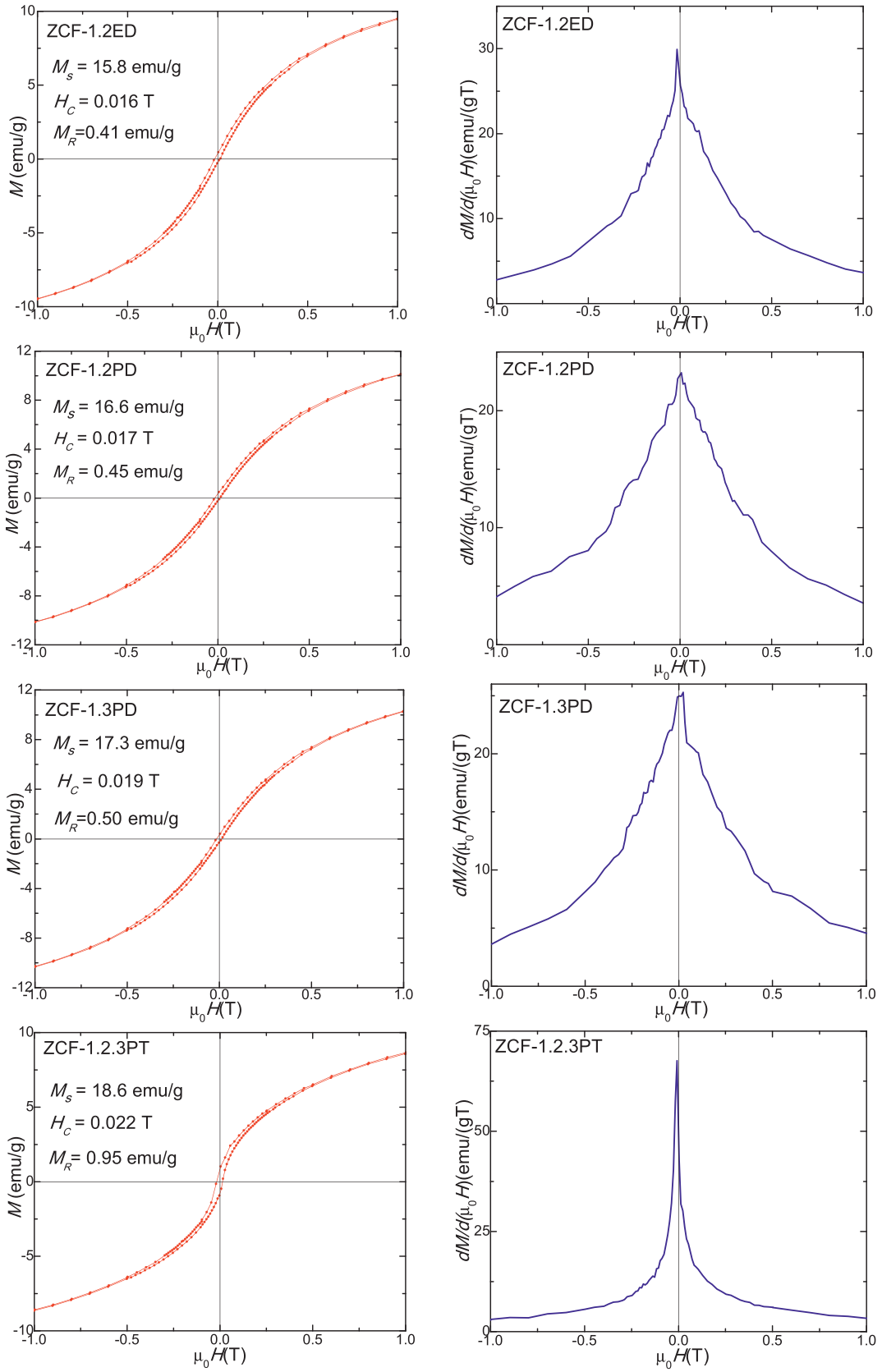

Fig. 5. Magnetic hysteresis loops and magnetization derivatives of $Zn_{0.5}Co_{0.5}Fe_2O_4/SiO_2$ NCs annealed at 700 °C.

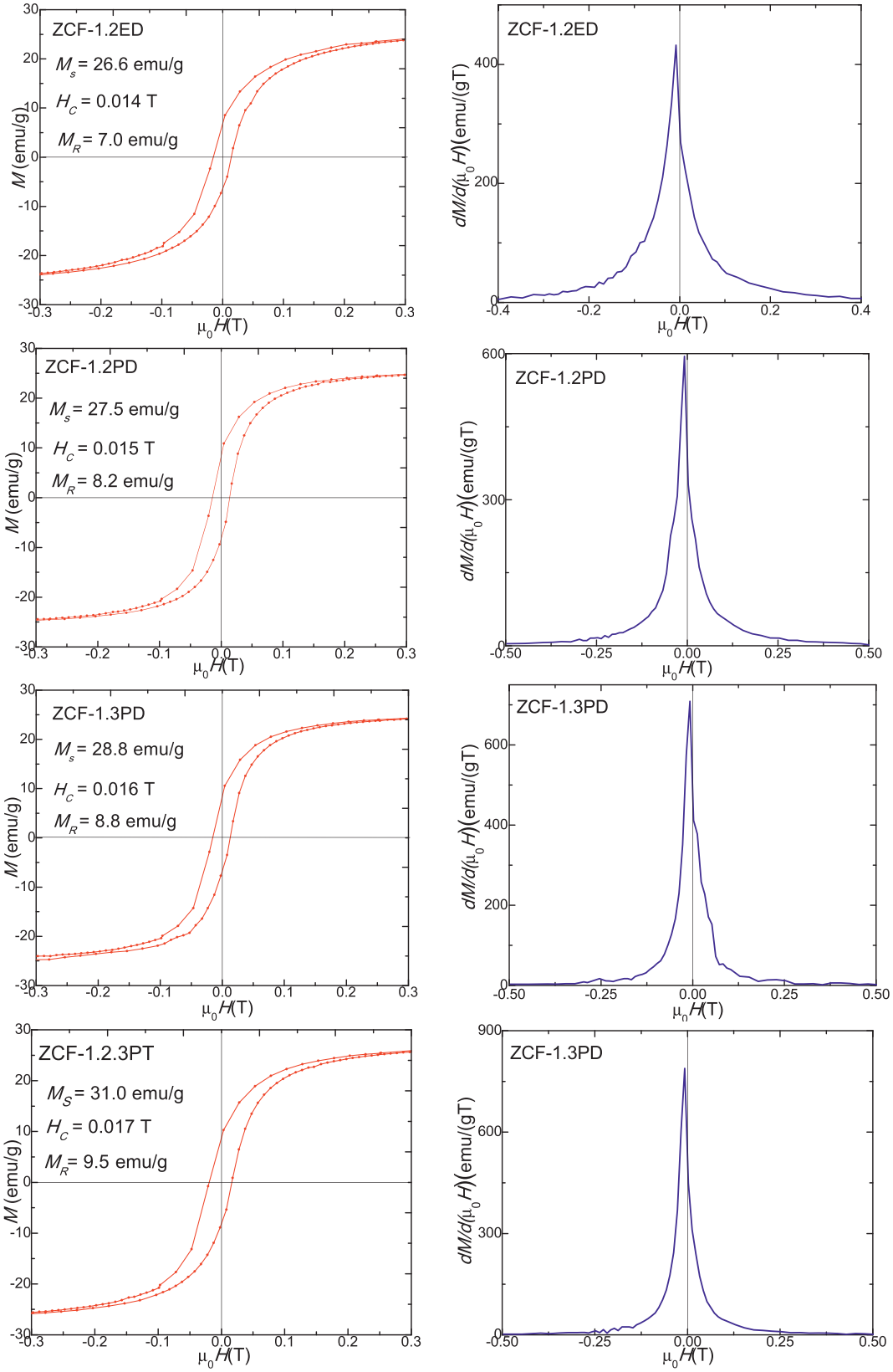

Fig. 6. Magnetic hysteresis loops and magnetization derivatives of $Zn_{0.5}Co_{0.5}Fe_2O_4/SiO_2$ NCs annealed at 1000 °C.

3.4. Magnetic properties of $Zn_{0.5}Co_{0.5}Fe_2O_4/SiO_2$ NCs

Saturation magnetization (M_s), coercivity (H_c) and remanent magnetization (M_R) obtained from magnetic hysteresis loops are very important parameters for the characterization of magnetic materials. Figs. 5 and 6 show the magnetic hysteresis loops and the magnetization derivatives (dM/d(μ_oH)) of NCs. The plots of dM/dH were taken from the descending magnetization curves. The hysteresis loops of

$Zn_{0.5}Co_{0.5}Fe_2O_4/SiO_2$ NCs annealed at 700 °C revealed a superparamagnetic-like behavior. This behavior results from the uncompensated spins of antiferromagnetic clusters which create giant effective spins that interact with the applied magnetic field [22]. Since the antiferromagnetic interactions are present both in intra- and inter-cluster spins, the global magnetic behaviours of these samples were found to be different from that of conventional superparamagnetic systems [22]. The hysteresis loops of ferrites annealed at 1000 °C indicate a ferromagnetic behaviour related to the distribution of Fe^{3+} and Co^{2+} ions within the lattice and related to crystallites size [22,39]. The M_R of NCs annealed at 700 °C has very low values and small variation (0.41–0.95 emu/g), while for NCs annealed at 1000 °C it exhibits larger values (7.0–9.5 emu/g).

In all the cases, M_s, H_c and M_R increase with the increasing distance between the hydroxyl groups and the number of hydroxyl groups. Moreover, M_s and M_R values considerably increase with increasing annealing temperature, while H_c has a negligible dependence on the annealing temperature. This behavior can be related to the influence of cationic stoichiometry and their distribution in the specific sites of the lattice, to the decrease of magnetocrystalline anisotropy, to the occupancy of magnetic cations sites and to the increase of random canting of particle surface spins [19,22]. The change of surface spins coordination creates an important change in the magnetic order of particles, due to the superexchange interaction mediated by oxygen ions and to the broken bonds when oxygen ions are missing from the surface [52]. The energy of a magnetic particle in an external field is proportional to the number of magnetic molecules in a single magnetic domain, and in consequence, to its size [22]. The presence of Zn^{2+} will result in the variation of the saturation magnetization intensity since the number of magnetic neighbours around Fe^{3+} is reduced, leading to uncoupled magnetic moments [53,54].

The H_c is strongly dependent on the average size of the particles. The presence of Co^{2+} ions in the Zn–Co ferrite is also important due to the non-zero orbital moment of Co^{2+} at octahedral sites. As known, the strong spin–orbit coupling has a high contribution to the magnetic anisotropy [53]. The distance between the hydroxyl groups of polyols and the number of hydroxyl groups only in a low increase of H_c attributed to the non-magnetic character of Zn^{2+} ions, depending on the composition. The H_c may increase as a consequence of the spin disorder at particle surface, which can enhance exchange anisotropy in the presence of various magnetic phases [19,55]. The H_c is strongly dependent on the magnetic anisotropy constant, defects and grain size [10].

Except for ZCF-1.2.3PT, the other NCs annealed at 700 °C have small and broad ($dM/d(\mu_0 H)$) versus applied magnetic field curves, suggesting partially crystalline samples and the presence of numerous crystal defects, dislocations and lattice strain. In case of NCs annealed at 1000 °C, these curves show sharp peaks, indicating the presence of a single magnetic phase. These diagrams do not reveal the presence of other magnetic phases besides Co-Zn-ferrite. This means that the secondary phases identified in XRD (Co_2SiO_4, Zn_2SiO_4, Co_3O_4, ZnO, SiO_2) have no magnetic properties (or they are present in very small quantities) and in consequence, have no influence on the paramagnetic and ferromagnetic properties of the NCs.

The dependence of M_S on the average particles size of the (D) (Fig. 7) is exponential (R^2 = 0.99918) for the NCs annealed at 700 °C and linear (R^2 = 0.99996) for NCs annealed at 1000 °C. This dependency is similar to that of the lattice parameter (a) on the average size of the particles (D), indicating that the saturation magnetization (M_S) has a similar behaviour to the lattice parameter (a). The ZCF-1.2EG annealed at 700 °C shows poor magnetic behaviour due to the superparamagnetic nature of Co^{2+} ions replacing the diamagnetic Zn^{2+} ions, while ZCF-1.2.3PT annealed at 1000 °C shows stable ferromagnetism, and it is a potential candidate for application in future spintronic and transparent nanodevices [43,54,55,56].

According to the results shown in Figs. 5–7 with increasing annealing temperature, there is a gradual growth in crystallinity and in particle size and hence the value of M_S also increases. This a well-known fact which mainly result from the surface to volume ratio effect in the nanoparticles [10,19,54]. The size effect also affects the M_S measurements, decreasing the contribution of the particles from the surface shell and enhancing the magnetization of samples annealed at high temperature [39].

4. Conclusions

In this paper, $Zn_{0.5}Co_{0.5}Fe_2O_4/SiO_2$ NCs were synthesized using 1,2-ethanediol (ZCF-1.2ED), 1,2-propanediol (ZCF-1.2PD), 1,3-propanediol (ZCF-1.3PD) and 1,2,3-propanetriol (ZCF-1.2.3PT) by a simple, fast and inexpensive sol–gel method. For all NCs, poorly crystalline $Zn_{0.5}Co_{0.5}Fe_2O_4$ at 700 °C and highly crystalline $Zn_{0.5}Co_{0.5}Fe_2O_4$ at 1000 °C, accompanied by other crystalline phases were identified. By annealing at 1000 °C, the formation of Co_2SiO_4 and Zn_2SiO_4 phases was also observed. The FT-IR spectra confirmed the formation of metal oxide bonds in Co-Zn ferrite and SiO_2 matrix. The lattice parameter shows increase at 700 and 1000 °C, following Vegard's law. The d_{phys} increases, while d_{XRD} and P decrease with the growing of the distance between the hydroxyl groups and number of hydroxyl groups and decrease with the annealing temperature. The decrease of P (17.866–16.124%, at 1000 °C) may be the result of the presence of different grain sizes since by annealing, the growth of the irregular shape grains takes place. The crystallites size increase with increasing distance between the hydroxyl groups and number of hydroxyl groups. TEM images showed highly agglomerated spherical particles, with size

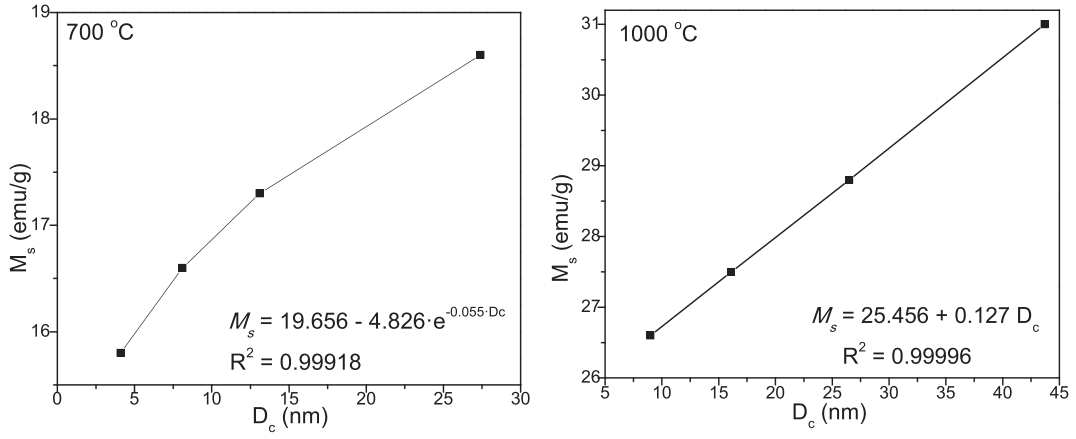

Fig. 7. Saturation magnetization (M_s) as a function of crystallite size (D_c) of $Zn_{0.5}Co_{0.5}Fe_2O_4/SiO_2$ NCs annealed at 700 and 1000 °C.

increasing from 2 to 10 nm (400 °C), 7 to 30 nm (700 °C) and 20 to 47 nm (1000 °C) as the distance between the hydroxyl groups grows. The hysteresis loops and magnetic properties (M_S, M_R, H_C) of $Zn_{0.5}Co_{0.5}Fe_2O_4/SiO_2$ NCs annealed at 700 °C indicate a superparamagnetic-like behavior (characterized by low magnetization values at 1 T, below 10 emu/g; low coercivity and very low magnetic remanence, below 1 emu/g). For the powders annealed at 1000 °C a ferromagnetic behaviour was revealed. The magnetic parameters such as M_S (26.6–31.0 emu/g), M_R (7.0–9.5 emu/g) and H_C (0.014–0.017 T) for $Zn_{0.5}Co_{0.5}Fe_2O_4$ NCs annealed at 1000 °C increase with increasing distance between the hydroxyl groups, suggesting ferromagnetic behavior which was explained, mainly, by making use of the surface spin disorder and canted spins effect. The M_S exponentially increases with the average crystallites size, for NCs annealed at 700 °C, while for NCs annealed at 1000 °C, the increase is linear. By controlling the synthesis method, the preparation conditions and annealing temperature, the magnetic properties of Zn-Co ferrite can be tuned to make it suitable for various applications. The obtained $Zn_{0.5}Co_{0.5}Fe_2O_4/SiO_2$ NCs have moderate magnetic properties which can be tuned to be used as potential candidates for magnetic electronics and optoelectronic applications.

Declaration of Competing Interest

The authors declare that they have no known competing financial interests or personal relationships that could have appeared to influence the work reported in this paper.

Acknowledgments

The support of Romanian Ministry of Economy by Sectorial Operational Program “Increase of Economic Competitiveness” Priority Axis II, Project Number 1887, INOVA-OPTIMA (O.C. and E.A.L.) and of Romanian Ministry of Research and Innovation, CNCS – UEFISCDI by grants PN-III-P1-1.1-MC-2018-0816 (O.C.), PN-III-P4-ID-PCE-2016-0534 and PN-III-P4-ID-PCCF-2016-0112 (I.G.D.) is greatly acknowledged. The authors would like to express their gratitude to Dr. Lucian Barbu Tudoran for the TEM measurements and to Dr. Razvan Hirian for the magnetic measurements.

References

[1] Y. Zhang, S.J. Park, Facile construction of MoO_3@ZIF-8 core-shell nanorods for efficient photoreduction of aqueous Cr (VI), Appl. Catal B: Environ. 240 (2019) 92–101.
[2] Y. Zhang, P. Soo-Jin, Formation of hollow MoO3/SnS2 heterostructured nanotubes for efficient light-driven hydrogen peroxide production, J. Mater. Chem. A 6 (2018) 20304–20312.
[3] Y. Zhang, P. Soo-Jin, Stabilization of dispersed CuPd bimetallic alloy nanoparticles on ZIF-8 for photoreduction of Cr(VI) in aqueous solution, Chem. Eng. J. 369 (2019) 353–362.
[4] Y. Zhang, S.J. Park, Incorporation of RuO_2 into charcoal-derived carbon with controllable microporosity by CO2 activation for high-performance supercapacitor, Carbon 122 (2017) 287–297.
[5] Y. Zhang, S.J. Park, Bimetallic AuPd alloy nanoparticles deposited on MoO_3 nanowires for enhanced visible-light driven trichloroethylene degradation, J. Catal. 361 (2018) 238–247.
[6] Y. Zhang, S.J. Park, Au–Pd bimetallic alloy nanoparticle-decorated $BiPO_4$ nanorods for enhanced photocatalytic oxidation of trichloroethylene, J. Catal. 355 (2017) 1–10.
[7] Y. Slimani, M.A. Almessiere, E. Hannachi, A. Baykal, A. Manikandan, M. Mumtaz, F. Ben, Azzouz, Influence of WO3 nanowires on structural, morphological and flux pinning ability of YBa2Cu3Oy superconductor, Ceram. Int. 45 (2019) 2621–2628.
[8] Y. Slimani, A. Baykal, A. Manikandan, Effect of Cr3+ substitution on AC susceptibility of Ba hexaferrite nanoparticles, J. Magn. Magn. Mater. 458 (2018) 204–212.
[9] Y. Slimani, E. Hannachi, A. Hamrita, M.K. Ben Salem, F. Ben Azzouz, A. Manikandan, M. Ben Salem, Comparative investigation of the ball milling role against hand grinding on microstructure, transport and pinning properties of $Y_3Ba_5Cu_8O_{18\pm\delta}$ and $YBa_2Cu_3O_{7-\delta}$, Ceram. Int. 44 (2018) 19950–19957.
[10] M. Atif, M.W. Asghar, M. Nadeem, W. Khalid, Z. Ali, S. Badshah, Synthesis and investigation of structural, magnetic and dielectric properties of zinc substituted cobalt ferrites, J. Phys. Chem. Solids 123 (2018) 36–42.
[11] A.-H. El Foulani, A. Aamouche, F. Mohseni, J.S. Amaral, D.M. Tobaldi, R.C. Pullar, Effect of surfactants on the optical and magnetic properties of cobalt-zinc ferrite $Co_{0.5}Zn_{0.5}Fe_2O_4$, J. Alloys Comp. 774 (2019) 1250–1259.
[12] A. Hanini, M. El Massoudi, J. Gavard, K. Kacem, S. Ammar, O. Souilem, Nanotoxicological study of polyol-made cobalt-zinc ferrite nanoparticles in rabbit, Environ. Toxicol. Pharmacol. 45 (2016) 321–327.
[13] J. Lopez, L.F. Gonzalez-Bahamon, J. Prado, J.C. Caicedo, G. Zambrano, M.E. Gomez, J. Esteve, P. Prieto, Study of magnetic and structural properties of ferrofluids based on cobalt–zinc ferrite nanoparticles, J. Magn. Magn. Mater. 324 (2012) 394–402.
[14] M. Ben Ali, K. El Maalam, H. El Moussaoui, O. Mounkachi, M. Hamedoun, R. Masrour, E.K. Hlil, A. Benyoussef, Effect of zinc concentration on the structural and magnetic properties of mixed Co–Zn ferrites nanoparticles synthesized by sol/gel method, J. Magn. Magn. Mater. 398 (2016) 20–25.
[15] A. Manikandan, M. Durka, S. Arul Antony, A novel synthesis, structural, morphological, and optomagnetic characterizations of magnetically separable spinel $Co_xMn_{1-x}Fe_2O_4$ ($0 \le x \le 1$) nano-catalysts, J Supercond. Nov. Magn 27 (12) (2014) 2841–2857.
[16] K. Elayakumar, A. Manikandan, A. Dinesh, K. Thanrasu, K. Kanmani Rajad, Y. Thilak Kumara, S.K. Slimani, A. Baykal Jaganathan, Enhanced magnetic property and antibacterial biomedical activity of Ce^{3+} doped $CuFe_2O_4$ spinel nanoparticles synthesized by sol-gel method, J. Magn. Magn. Mater. 478 (2019) 140–147.
[17] K. Elayakumar, A. Dinesh, A. Manikandan, M. Palanivelu, G. Kavitha, S. Prakash, R. Thilak Kumar, S.K. Jaganathan, A Baykal, Structural, morphological, enhanced magnetic properties and antibacterial bio-medical activity of rare earth element (REE) cerium (Ce^{3+}) doped $CoFe_2O_4$ nanoparticles, J. Magn. Magn. Mater. 476 (2019) 157–165.
[18] Y. Slimani, M.A. Almessiere, E. Hannachi, M. Mumtaz, A. Manikandan, A. Baykal, F. Ben Azzouz, Improvement of flux pinning ability by tungsten oxide nanoparticles added in $YBa_2Cu_3O_y$ superconductor, Ceram. Int. 45 (2019) 18683–18690.
[19] K. Nadeem, M. Shahid, M. Mumtaz, Competing crystallite size and zinc concentration in silica coated cobalt ferrite nanoparticles, Prog. Nat. Sci-Mater. 24 (2014) 199–204.
[20] A. Poorbafrani, E. Kiani, Enhanced microwave absorption properties in cobalt–zinc ferrite based nanocomposites, J. Magn. Magn. Mater. 416 (2016) 10–14.
[21] M. Chithra, C.N. Anumol, B. Sahu, S.C. Sahoo, Structural and magnetic properties of $Zn_XCo_{1-X}Fe_2O_4$ nanoparticles: nonsaturation of magnetization, J. Magn. Magn. Mater. 424 (2017) 174–184.
[22] F. Gözüak, Y. Köseoğlu, A. Baykal, H. Kavas, Synthesis and characterization of $Co_xZn_{1-x}Fe_2O_4$ magnetic nanoparticles via a PEG-assisted route, J. Magn. Magn. Mater. 321 (2009) 2170–2177.
[23] A.V. Raut, R.S. Barkule, D.R. Shengule, K.M. Jadhav, Synthesis, structural investigation and magnetic properties of Zn^{2+} substituted cobalt ferrite nanoparticles prepared by the sol–gel auto-combustion technique, Magn. Magn. Mater. 358–359 (2014) 87–92.
[24] I.G. Deac, R. Tetean, I. Balasz, E. Burzo, Low-temperature magnetic ordering in the perovskites $Pr_{(1-x)}A_{(x)}CoO_{(3)}$ (A = Ca, Sr), J. Magn. Magn. Magn. 322 (2010) 1185–1188.
[25] A. Manikandan, Vijaya, J. Judith, Kennedy, L. Joh, Structural Optical and magnetic properties of porous α-Fe_2O_3 nanostructures prepared by rapid combustion method, J. Nanosci. Nanotechnol. 13 (4) (2013) 2986–2992.
[26] S. Asiri, M. Sertkol, S. Guner, H. Gungunes, K.M. Batoo, T.A. Saleh, H. Sozerig, M.A. Almessiere, A. Manikandan, A. Baykal, Hydrothermal synthesis of $Co_yZn_yMn_{1-2y}Fe_2O_4$ nanoferrites: magneto-optical investigation, Ceri. Int. 44 (5) (2018) 5751–5759.
[27] A. Manikandan, R. Sridhar, S. Arul Antony, Seeram Ramakrishna, A simple aloe vera plant-extracted microwave and conventional combustion synthesis: morphological, optical, magnetic and catalytic properties of $CoFe_2O_4$ nanostructures, J. Mol. Struct. 1076 (2014) 188–200.
[28] A. Manikandan, M. Durka, K. Seevakan, S. Arul Antony, A novel one-pot combustion synthesis and optomagnetic properties of magnetically separable spinel $Mn_xMg_{1-x}Fe_2O_4$ ($0.0 \le x \le 0.5$) nanophotocatalysts, J. Supercond. Nov. Magn. 28 (4) (2015) 1405–1416.
[29] T. Dippong, E.A. Levei, O. Cadar, Preparation of $CoFe_2O_4/SiO_2$ nanocomposites at low temperatures using short chain diols, J. Chem. (2017) 7943164.
[30] T. Dippong, O. Cadar, E.A. Levei, I.G. Deac, F. Goga, G. Borodi, L. Barbu-Tudoran, Influence of polyol structure and molecular weight on the shape and properties of $Ni_{0.5}Co_{0.5}Fe_2O_4$ nanoparticles obtained by sol-gel synthesis, Ceram. Int. 45 (2019) 7458–7467.
[31] S.B. Rice, C. Chan, S.C. Brown, P. Eschbach, L. Han, D.S. Ensor, A.B. Stefaniak, J. Bonevich, A.E. Vladar, A.R. Hight Walker, J. Zheng, C. Starnes, A. Stromberg, J. Ye, E.A. Grulke, Particle size distributions by transmission electron microscopy: an interlaboratory comparison case study, Metrologia 50 (2013) 663–678.
[32] Joint Committee on Powder Diffraction Standard, International Center for Diffraction Data, 1999.
[33] A.H. Ashour, A.I. El-Batal, M.I.A. Maksouda, G.S. El-Sayyad, S. Labib, E. Abdeltwab, M.M. El-Okr, Antimicrobial activity of metal-substituted cobalt ferrite nanoparticles synthesized by sol–gel technique, Particuology 40 (2018) 141–151.
[34] T. Dippong, O. Cadar, E.A. Levei, I.G. Deac, L. Diamandescu, L. Barbu Tudoran, Influence of cobalt ferrite content on the structure and magnetic properties of $CoFe_2O_4)_X(SiO_2$-$PVA)_{100-X}$ nanocomposites, Ceram. Int. 44 (2018) 7891–7901.
[35] R.R. Powar, V.D. Phadtare, V.G. Parale, H.-H. Park, S. Pathak, P.R. Kamble, P.B. Piste, D.N. Zambare, Structural, morphological, and magnetic properties of $Zn_xCo_{1-x}Fe_2O_4$ ($0 \le x \le 1$) prepared using a chemical co-precipitation method, Ceram. Int. 44 (2018) 20782–20789.
[36] M. Amir, H. Gungunes, Y. Slimani, N. Tashkandi, H.S. El Sayed, F. Aldakheel, M. Sertkol, H. Sozeri, A. Manikandan, I. Ercan, A. Baykal, Mössbauer studies and

magnetic properties of cubic $CuFe_2O_4$ nanoparticles, J Supercond. Nov. Magn. 32 (2019) 557–564.
[37] A.D. Korkmaz, S. Güner, Y. Slimani, H. Gungunes, Md Amir, A. Manikandan, A. Baykal, Microstructural, optical, and magnetic properties of vanadium-substituted nickel spinel nanoferrites, J Supercond. Nov. Magn. 32 (2019) 1057–1065.
[38] S. Asiri, M. Sertkol, H. Güngüneş, M. Amir, A. Manikandan, İ. Ercan, A. Baykal, The temperature effect on magnetic properties of $NiFe_2O_4$ nanoparticles, J. Inorg. Organomet. Polym. 28 (2018) 1587–1597.
[39] E. Swatsitang, S. Phokha, S. Hunpratub, B. Usher, A. Bootchanont, S. Maensiri, P. Chindaprasirt, Characterization and magnetic properties of cobalt ferrite nanoparticles, J. Alloys Comp. 664 (2016) 792–797.
[40] V.G. Patil, S.E. Shirsath, S.D. More, S.J. Shukla, K.M. Jadhav, Effect of zinc substitution on structural and elastic properties of cobalt ferrite, J. Alloys Comp. 488 (2009) 199–203.
[41] T.R. Tatarchuk, M. Bououdina, N.D. Paliychuk, I.P. Yaremiy, V.V. Moklyak, Structural characterization and antistructure modeling of cobalt substituted zinc ferrites, J. Alloys Comp. 694 (2017) 777–791.
[42] G. Barrera, M. Coisson, F. Celegato, S. Raghuvanshi, F. Mazaleyrat, S.N. Kane, P. Tiberto, Cation distribution effect on static and dynamic magnetic properties of $Co_{1-x}Zn_xFe_2O_4$ ferrite powders, J. Magn. Magn. Mater. 456 (2018) 372–380.
[43] T. Dippong, E.A. Levei, O. Cadar, F. Goga, L. Barbu Tudoran, G. Borodi, Size and shape-controlled synthesis and characterization of $CoFe_2O_4$ nanoparticles embedded in a PVA-SiO_2, J. Anal. Appl. Pyrol. 128 (2017) 121–130.
[44] S. Nazim, T. Kousar, M. Shahid, M.A. Khan, G. Nasar, M. Sher, M.F. Warsi, New graphene-$Co_xZn_{1-x}Fe_2O_4$ nano-heterostructures: magnetically separable visible light photocatalytic materials, Ceram. Int. 42 (2016) 7647–7654.
[45] T. Dippong, E.A. Levei, C. Tanaselia, M. Gabor, M. Nasui, L. Barbu Tudoran, G. Borodi, Magnetic properties evolution of the $Co_xFe_{3-x}O_4/SiO_2$ system due to advanced thermal treatment at 700 °C and 1000 °C, J. Magn. Magn. Mater. 410 (2016) 47–54.
[46] B.C. Babu, S. Buddhudu, Analysis of structural and electrical properties of Ni^{2+}:Zn_2SiO_4 ceramic powders by sol–gel method, J. Sol-Gel Sci. Technol. 70 (3) (2014) 405–415.
[47] T. Dippong, I.G. Deac, O. Cadar, E.A. Levei, G. Borodi, L. Diamandescu, Effect of Zn content on structural, morphological and magnetic behavior of $Zn_xCo_{1-x}Fe_2O_4/SiO_2$ nanocomposites, J. Alloys Comp. 792 (2019) 432–443.
[48] T. Dippong, F. Goga, E.A. Levei, O. Cadar, Influence of zinc substitution with cobalt on thermal behaviour, structure and morphology of zinc ferrite embedded in silica matrix, J. Solid State Chem. 275 (2019) 159–166.
[49] S.Y. Zhao, D.K. Lin, C.W. Kim, I.L.G. Cha, Y.I.I. Kim, Y.S. Kang, Synthesis of magnetic nanoparticles of Fe_3O_4 and $CoFe_2O_4$ and their surface modification by surfactant adsorption, Bull. Korean Chem. Soc. 27 (2006) 237–242.
[50] C.C. Wang, J.M. Lin, C.R. Lin, S.C. Wang, Preparation and application of hollow silica/magnetic nanocomposite, Intern. J. Mod. Phys: Conf. Ser. 6 (2012) 601–609.
[51] K. Winiarska, R. Klimkiewicz, W. Tylus, A. Sobianowska-Turek, J. Winiarski, B. Szczygieł, I. Szczygieł, Study of the catalytic activity and surface properties of manganese-zinc ferrite prepared from used batteries, J. Chem. 2019 (2019) 1–14, https://doi.org/10.1155/2019/5430904.
[52] M.H. Yousefi, S. Manouchehri, A. Arab, M. Mozaffari, G.R. Amiri, J. Amighian, Preparation of cobalt–zinc ferrite ($Co_{0.8}Zn_{0.2}Fe_2O_4$) nanopowder via combustion method and investigation of its magnetic properties, Mater. Res. Bull. 45 (2010) 1792–1795.
[53] Z.-H. Chen, Y.-P. Sun, Z.-T. Kang, D. Chen, Preparation of $Zn_xCo_{1-x}Fe_2O_4$ nanoparticles by microwave-assisted ball milling, Ceram. Int. 40 (2014) 14687–14692.
[54] M. Zamani, E. Naderi, M. Aghajanzadeh, M. Naseri, A. Sharafi, H. Danafar, $Co_{1-x}Zn_xFe_2O_4$ based nanocarriers for dual-targeted anticancer drug delivery: synthesis, characterization and in vivo and in vitro biocompatibility study, J. Molec. Liq. 274 (2019) 60–67.
[55] A. Hirohata, H. Sukegawa, H. Yanagihara, I. Žutić, T. Seki, S. Mizukami, R. Swaminathan, Roadmap for emerging materials for spintronic device applications, IEEE Trans. Magn. 51 (2015) 0800511.
[56] M.S. Tomar, S.P. Singh, O. Perales-Perez, R.P. Guzman, E. Calderonc, C. Rinaldi-Ramos, Synthesis and magnetic behavior of nanostructured ferrites for spintronics, Microelectron. J. 36 (2005) 475–479.